University of Groningen

Strong gravitational lensing in the radio domain

Berciano Alba, Alicia

IMPORTANT NOTE: You are advised to consult the publisher's version (publisher's PDF) if you wish to cite from it. Please check the document version below.

Document Version
Publisher's PDF, also known as Version of record

Publication date:
2009

Citation for published version (APA):
Berciano Alba, A. (2009). *Strong gravitational lensing in the radio domain*. s.n.

4

New evidence for the merger scenario in SMM J04542−0301

SMM J04542−0301 is an extended (∼ 1′) sub-mm source located near the core of the cluster MS0451.6−0305. It has been suggested that part of its emission arises from the interaction between a LBG and two EROs at z ∼ 2.9 that are multiply-imaged. However, the dramatic resolution difference between the sub-mm map and the optical/NIR images make it difficult to confirm this hypothesis. In this Chapter, we present a deep (∼ 10 μJy beam^{-1}), high resolution (∼ 2″) 1.4 GHz radio map of the cluster core, in which we have identified 6 sources located within SMM J04542−0301. The strong lensing effect in the radio data has been quantified by constructing a new lens model of the cluster. The brightest and most extended of these sources (RJ) is located in the middle of the sub-mm emission, and has no obvious counterpart in the optical/NIR. Three other detections (E1, E2 and E3) seem to be associated with the images of one of the EROs (B), although the NIR and radio emission appear to originate at slightly different positions in the source plane. The last two detections (CR1 and CR2), for which no optical/NIR counterpart have been found, seem to constitute two relatively compact emitting regions embedded in a ∼ 5″ extended radio source located at the position of the sub-mm peak. The presence of this extended component can only be explained if it is being produced by a lensed region of dust obscured star formation in the center of the merger. A comparison between the radio and sub-mm data at the same resolution suggests that E1, E2, E3, CR1 and CR2 are associated with the sub-mm emission. These radio observations provide strong observational evidence in favor of the merger hypothesis. However, the question if RJ is also contributing to the observed sub-mm emission remains open. These results illustrate the promising prospects for radio interferometry and strong gravitational lensing to study the internal structure of sub-mm galaxies.

4.1   Introduction

The detection of the cosmic infrared background (CIB) by the COBE satellite (Puget et al. 1996; Hauser et al. 1998) established that about half of the total radiation in the universe comes from dust-obscured galaxies that are missing from optical surveys (see Lagache et al. 2005, for a review). This population of dusty objects was first resolved by the IRAS and ISO satellites up to $z \sim 1$, and turned out to be dominated by luminous and ultra-luminous IR galaxies (LIRGs and ULIRGs). The step into the high-z universe came with the advent of sub-mm and mm surveys, since the far-infrared (FIR) luminosity peak of high-z obscured galaxies is red-shifted into the sub-mm band (Franceschini et al. 1991; Blain & Longair 1993). As a result, sub-mm galaxies (hereafter SMGs) turned out to be hundreds of times more numerous than galaxies with similar luminosities in the local universe, suggesting that they constitute the dominant contributor of the CIB and cosmic star formation at $z \gtrsim 1$. This illustrates the very important role that SMGs play in the context of galaxy formation and evolution (see Lonsdale et al. 2006, for a review on (U)LIRGs and SMGs).

One decade after their discovery with SCUBA[1] (Smail et al. 1997; Hughes et al. 1998; Barger et al. 1998; Eales et al. 1999), it is generally accepted that SMGs are heavily dust-obscured galaxies at high redshift ($2 < z < 3$) with ULIRG-like luminosities ($L_{\mathrm{FIR}} \sim 10^{12} \, L_\odot$) and star formation rates of the order of $1000 \, M_\odot \, yr^{-1}$. This enormous bolometric luminosity seems to be dominated by star formation processes induced by galaxy interactions/mergers, although a good fraction ($\sim 30 - 50\%$) of SMGs also host AGN activity (Alexander et al. 2005). First estimates of their physical properties indicate that SMGs are massive, gas rich systems ($M_{\mathrm{gas}} \sim 10^{10} - 10^{11} \, M_\odot$) in which the starburst region has a typical scale in the range $1 - 8$ kpc (Neri et al. 2003; Chapman et al. 2004; Greve et al. 2005; Tacconi et al. 2006; Wang et al. 2007; Biggs & Ivison 2008). The available evidence also suggests that SMGs might be the progenitors of massive local ellipticals (Lilly et al. 1999; Smail et al. 2002, 2004; Webb et al. 2003; Genzel et al. 2003; Alexander et al. 2003, 2005; Swinbank et al. 2006b).

However, these general properties of SMGs are based on the study of the very brightest examples of this class of object ($S_{850\mu m} \gtrsim 2$ mJy), and may not be representative of the entire SMG population. In fact, according to Knudsen et al. (2008), the dominant contribution to the sub-mm extragalactic background comes from the fainter (sub-)mJy sources that cannot usually be detected due to the confusion noise of current instruments ($S_{850\mu m} \sim 2$ mJy). The only way in which it has been possible to push bellow this sensitivity limit, is by using the lensing magnification provided by massive clusters of galaxies to increase the effective resolution of SCUBA. This approach has improved the sensitivity of sub-mm maps by factors of a few with respect to blank field surveys, although just a handful of faint SMGs have being identified so far (Smail et al. 2002; Cowie et al. 2002; Knudsen et al. 2008). Since so little is known about these intrinsically faint sources, it is crucial to further investigate their properties (e.g. spectral energy distributions (SEDs), morphologies, redshifts, etc.) and assess whether they are different from the observed properties of brighter SMGs.

---

[1]Sub-millimeter Common-User Bolometer Array, decommissioned in September 2005 from the James Clerk Maxwell Telescope on Mauna Kea.
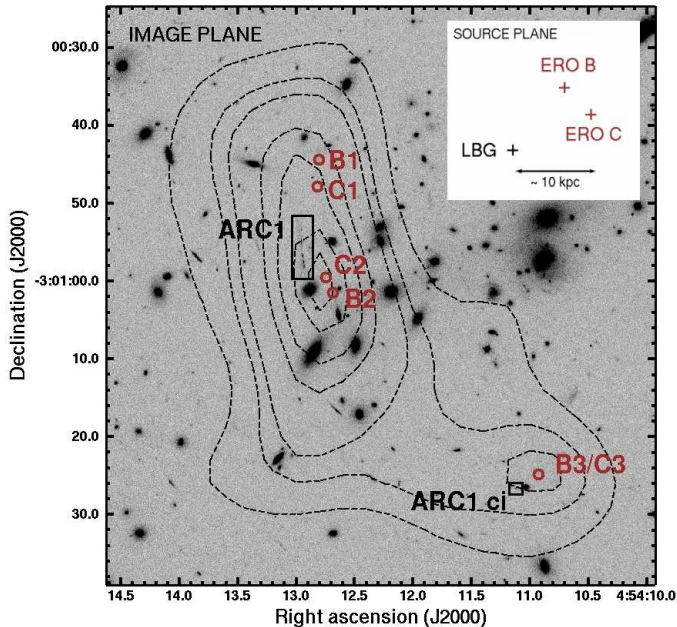
Figure 4.1: *Summary of the results presented in Borys et al. (2004a).* *SCUBA* 850 μm
contour map of SMM J04542−0301 superimposed upon a HST image of the center of the
cluster MS0451.6−0305. Highlighted with rectangles are an optical arc (ARC1) and its counter
image (ARC1 ci), produced by a LBG at z_{spect} = 2.911. *The red circles indicate the positions of*
five NIR sources that have been interpreted as multiple images produced by two EROs (ERO
B, lensed as B1/B2/B3, and ERO C, lensed as C1/C2/C3) at z_{model} = 2.85 ± 0.1. *Assuming* z = 2.9
for both the LBG and the EROs, their predicted positions in the source plane would be located
withing a region of ∼ 10 kpc, *suggesting that they constitute a merger.*

A promising strategy to gather information about faint SMGs is to study members
that are multiply imaged by clusters of galaxies. In this cases, the magnification factor
can go up to 30 (or more), providing not only the opportunity to detect but also to
spatially resolve the morphologies and internal dynamics of faint SMGs at a level of
detail far greater than would otherwise be possible (see Swinbank et al. 2007, for an
example of this technique in the optical). To date, only one multiply-imaged faint
SMGs has been confirmed: SMM J16359+6612, located near the core of the cluster
A2218 (Kneib et al. 2004b, 2005; Garrett et al. 2005; Knudsen et al. 2008, 2009). There
are, however, two other clusters which seem to host multiply-imaged SMGs: A1689
(Knudsen et al. 2008) and MS0451.6−0305 (Chapman et al. 2002a; Borys et al. 2004a;
Berciano Alba et al. 2007).

The case of MS0451.6−0305 is particularly interesting, since the "sub-mm source"
(SMM J04542−0301) is an elongated (∼ 1') region of 850 μm emission which is coinci-
dent with an optical arc and five NIR sources (see Fig. 4.1). While the optical arc is the
result of a strongly-lensed Lyman Break Galaxy (LBG) at z_{spect} = 2.911, a lens model

of the cluster predicts that the set of NIR sources could be produced by two triply-imaged EROs located at almost the same redshift ($z_{model} = 2.85 \pm 0.1$). The model also indicates that the ERO pair and the LBG may constitute a merger at z = 2.9 in the source plane, with their interaction likely being at the origin of the observed sub-mm emission (Borys et al. 2004a, B04 hereafter). Unfortunately, the low resolution ($\sim 15''$ at 850 μm) and poor positional accuracy ($\sim 2'' - 3''$ rms) of SCUBA, makes it very difficult to confirm the link between SMM J04542−0301 and the proposed optical/NIR sources. Moreover, the emission coming from the north-eastern and central regions of the sub-mm emission cannot be reproduced by the arc and the NIR sources (see Fig. 7 in B04), suggesting that it might arise via other sources.

A possible way to overcome this resolution problem is by taking advantage of the observed correlation between the radio synchrotron and FIR emission in star-forming galaxies (van der Kruit 1973; Condon et al. 1982; Helou et al. 1985; Garrett 2002; Appleton et al. 2004; Beelen et al. 2006), which also seems to hold for SMGs out to $z \sim 3$ (Kovács et al. 2006; Vlahakis et al. 2007; Ibar et al. 2008; Michałowski et al. 2009). Thanks to this *FIR-radio correlation*, radio interferometric observations can be used as a high-resolution proxy for the rest-frame FIR emission observed in the sub-mm. This approach has been extensively used to pinpoint the position of SMGs in order to identify their faint optical counterparts (e.g. Ivison et al. 2000; Barger et al. 2000; Chapman et al. 2005; Ivison et al. 2007).

In the third Chapter of this thesis, we reported the detection of 1.4 GHz radio emission coincident with SMM J04542−0301 using VLA[2] archival data. Part of this radio emission is located in the region between the optical arc and the ERO images, which is consistent with the interacting region of the hypothetical merger being the source of the observed radio and sub-mm emission. We also detected bright radio emission in the central region of SMM J04542−0301, although it was not clear if this emission is produced by a high-z lensed object or AGN activity associated with a cluster member.

In this Chapter, we present a higher resolution 1.4 GHz radio map of the center of the cluster MS0451.6−0305 (MS0451 hereafter), obtained after combining the previous VLA archival data (BnA configuration) with new VLA high resolution observations (A configuration). The details of both sets of observations are presented in Sect. 2, together with a description of the data analysis procedure, which has been considerably improved with respect to the previous Chapter. Section 3 is dedicated to the analysis of the final combined data set, from which we characterize the compact and extended radio emission detected within SMM J04542−0301. Identification of optical (HST/ACS F814W) and NIR (SUBARU/CISCO K' band) counterparts for the radio detections, as well as their connection with the sub-mm emission, is discussed in Sect. 4. In Sect. 5 we describe a new lens model of the cluster MS0451, built to investigate the lensed nature of the compact radio detections. A discussion about the merger scenario proposed by B04, including the results from the radio observations, is presented in Sect. 6. Summary and conclusions are presented in Sect. 7.

The adopted cosmology corresponds to a ΛCDM model with $\Omega_m = 0.28, \Omega_\lambda = 0.72$ and $h_0 = 73$ (Spergel et al. 2007).

---

[2]Very Large Array interferometer of the National Radio Astronomy Observatory (NRAO)

4.2   Radio Observations and Data Reduction

The 1.4 GHz observations of the cluster MS0451 presented in this Chapter were obtained with the VLA in A and B configurations (A-array and B-array hereafter) using the wide-field *pseudo-continuum mode*. This mode consists on two IFs of 25 MHz, centered at 1.3649 GHz and 1.4351 GHz. Each IF contains right and left circular polarizations and it is split into seven 3.125 MHz channels. The absolute flux density scale was set by the flux calibrator $0137 + 331$ (3C48), while $0503 + 020$ was used as the phase calibrator (PHCS hereafter). The data reduction was conducted in classic AIPS using our own semi-automatic pipeline written in *Parseltongue* (Python interface to classic AIPS, see Kettenis et al. 2006).

4.2.1   A-array Observations

The A-array observations consist on 2×6 hours of data acquired the 5th and 10th of February 2006 (correlator integration time of 3.3 seconds). Each IF of each observing day was independently self-calibrated, resulting in four data sets that were in the end combined to obtain the final A-array map of the target. In order to avoid source smearing, no averaging in frequency nor time was applied to the data. The different steps followed during the data reduction of each epoch are described next.

First, we improved the positional accuracy of the antennas in our data by applying the most recent baseline corrections determined by NRAO. Corrupted data were visually inspected and flagged independently for each channel, IF and polarization at different stages of the data reduction process.

To set the flux scale, amplitude and phase corrections were calculated for 3C48 using a model of this source provided by AIPS. Then, 3C48 was used to calibrate the bandpass shape. In the case of the PHCS, we first derived a preliminary calibration in amplitude and phase using a point source model. Subsequent self-calibration produced a more accurate clean component model (CC model hereafter), which was ultimately used to derive the final phase calibration. After proper interpolation, the resultant amplitude and phase solutions were applied to the cluster data, and further refined through self-calibration in order to produce the optimal map for our target.

Figure 4.2 (top) shows a low resolution 1×1 deg map of the cluster produced with the inner 10 kλ baselines of the A-array data. Due to the significant number of bright sources located outside the main lobe of the primary beam (black circle), 37 facets were used for the imaging part of the self-calibration process: 31 overlapping facets that cover the central 0.32 deg radius region, and 6 individual facets centered at the positions of bright NVSS sources[3] located in an annulus between 0.32 and 0.5 deg. radius. The size of each facet is 2048×2048 pixels, with a pixel scale of 0.247″. Areas for CLEANING were restricted by placing boxes around the brightest sources in each facet. The weighting scheme used for imaging was selected by the IMAGR parameter ROBUST (R hereafter), with value ranging from +5 (pure natural weighting) to −5 (pure uniform weighting). To produce a good model of the compact emission, R = 0 was

---

[3]The NRAO VLA Sky Survey (NVSS) is a 1.4 GHz continuum survey covering the entire sky north of −40 deg. declination, with a completeness limit about 2.5 mJy
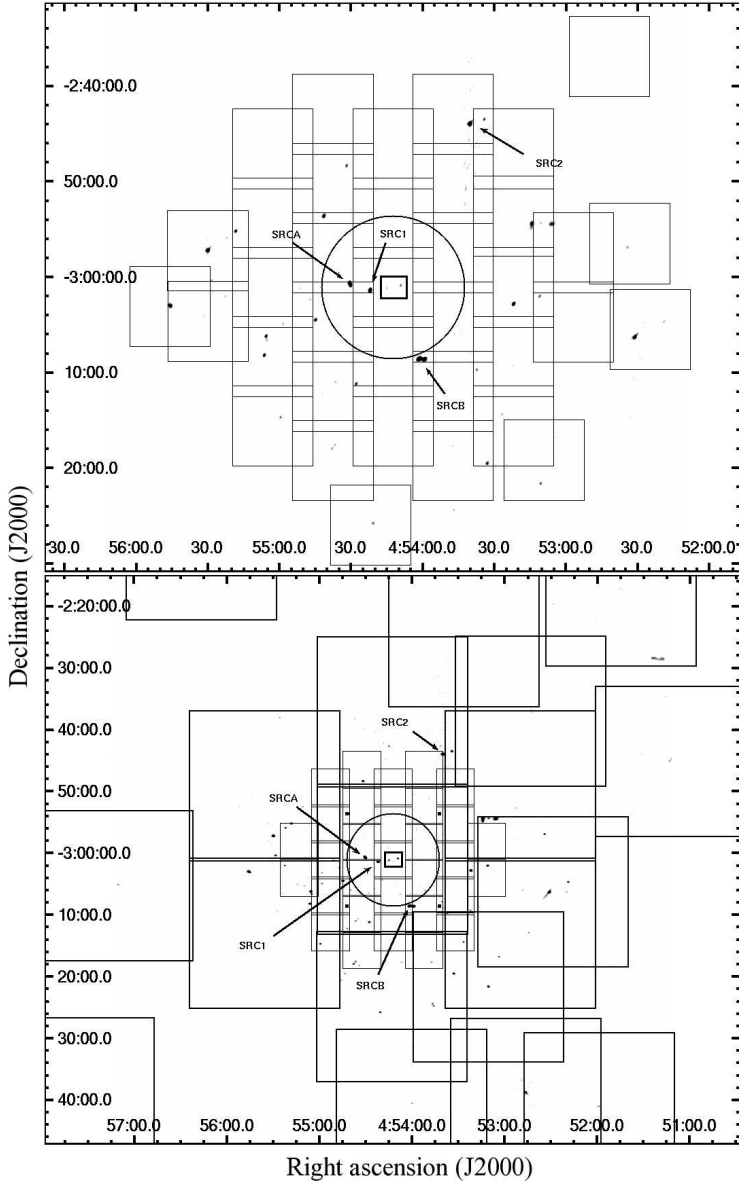
Figure 4.2: *VLA 1.4 GHz maps centered in the core of the cluster MS0451.6−0305. The maps were produced using the visibilities of the central 10 kλ region of the UV-plane only, to enhance the source visibility. The facets used during the selfcalibration of the cluster data are indicted with boxes, while the circle represents the VLA FWHM primary beam (0.25°. at 1.4 GHz). The central bold box corresponds to the target region mapped in Fig. 4.4. The brightest sources in the field are indicated with labels. **Top Panel:** 1° × 1° map produced with the A-array observations. Each box is 8.4′ × 8.4′. **Bottom Panel:** 1.5° × 1.5° map produced with the B-array observations. The big boxes (used in the first step of the selfcalibration procedure) are 27.8′ × 27.8′ in size, whereas the small boxes (used in the second step) are 6.8′ × 6.8′.*

used until the last iteration of the self-calibration procedure, where we switched to R = 5 to include the extended emission.

From the sources indicated in the top panel of Fig. 4.2, SRC1 is compact, and it is the brightest and closest to the target, so it should provide the best self-calibration solutions in the target region. However, the extended sources SRCA and SRCB dominate the solutions in the short baselines. In order to get the final calibration only from SRC1 for all baselines, all the sources located outside the central facet were subtracted from the data using the final CC model of the outer 37 facets. Finally, the resultant data set was self-calibrated again using R = 5 during the imaging process.

This procedure was followed for each IF of each epoch, resulting in four independently calibrated data sets (in which only the sources from the central facet remain) that were concatenated with DBCON to produce the final A-array map of the target.

4.2.2   B-array Observations

The B-array observations, made the 9th and 10th of June 2002, were retrieved from the NRAO data archive system[4] (7.8 hours in total, correlator integration time of 10 seconds). In Chapter 3, these observations were treated as a single epoch and averaged in time, with no independent calibration for each IF. However, since our goal is to combine the data from both array configurations to produce a more sensitive map of the target, the B-array observations were re-reduced following essentially the same procedure described in the previous section. The only difference corresponds to the self-calibration of the cluster data, which we now describe in detail.

Figure 4.2 (bottom) shows a 1.5×1.5 deg low resolution map of the cluster produced with the inner 10 Kλ baselines of the B-array data. Note that SRC2 is brighter than SRC1, contrary to the situation in the A-array data (top) where SRC2 is resolved. However, since SRC2 is considerably further away from the phase center, the best self-calibration solutions on the target region will still be provided by SRC1. Therefore, the data was self-calibrated in three steps. First, a set of 7 overlapping facets was used to image the central 0.4 deg radius region of the data, while another 36 facets were centered at the positions of NVSS sources located in an annulus between 0.4 and 1.6 deg radius (big boxes in the bottom panel of Fig. 4.2). Each facet is 2048×2048 pixels, with a pixels size of 0.814″. Once the self-calibration procedure was completed, the CC model from the 42 outer facets was subtracted from the data, leaving only the sources located in the central facet. In the second step, the central region of the resultant data set is imaged again using 31 overlapping facets of 500×500 pixels. After following the same self-calibration procedure used in the first step, the best CC model of the outer 30 facets was subtracted from the data. In the third step, this final data set is calibrated (phase only) using a solution interval of 5 min and R = 5.

As in the case of the A-array observations, the four independently calibrated data sets obtained in this way (one per epoch and IF) were then combined and imaged to produce the final B-array map of the target.

---

[4]Project ID AN0109, PI: Nakanishi
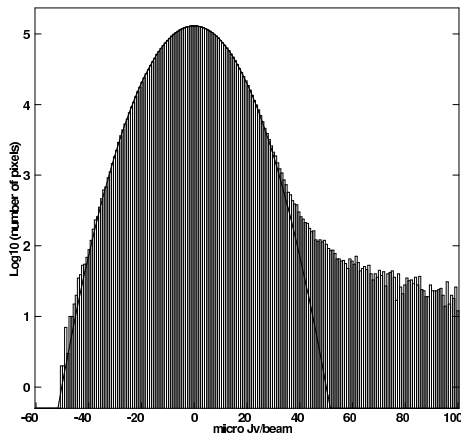
Figure 4.3: *Histogram of the A+B array clean map produced using* R = 0.6. *The black curve is the best Gaussian fit to the noise peak, while the positive excess on the right side is due to source emission. The good agreement between the fit and the data in the negative side of the Gaussian indicates that the noise of the map is well behaved, making faint detections more reliable.*

4.3   Analysis of the A+B-array map

Before the A-array and B-array observations could be combined to produce the final radio map of the cluster center, it was necessary to correct for a single position shift between the two calibrated data-sets. This correction was achieved by performing a global phase-selfcalibration of the B-array data set using the best A-array CC model.

To produce the map with the best compromise between sensitivity and noise properties, we explored the full range of values available for the IMAGR parameter ROBUST. The histograms of the resultant clean maps show that the noise distribution is closest to Gaussian when R = 0.6 (see Fig. 4.3). Note also that the rms noise of the R = 0.6 map ($\sim 10\ \mu$Jy) is only 2% higher than the one obtained for R = 5, which is the most sensitive map that can be produced with this data.

4.3.1   Catalog of radio sources

Figure 4.4 shows a detail on the R = 0.6 map of the cluster center produced by cleaning the data down to a depth of 5.5 μJy. The contours indicate the region of extended sub-mm emission reported by B04, in which six of the eight identified radio sources are located. Postage stamps of these six sources and their CC models are shown in Fig. 4.5.

The radio detections located outside the sub-mm emission, labeled Fd and Fe, are the same sources reported in Chapter 3. Their morphology in the new high resolution radio map is very elongated, typical of radio jets produced by AGNs. In the case of the other 6 sources, the morphology and distribution of their clean components show that, with the exception of the (almost) point-like structure of E1, the rest of
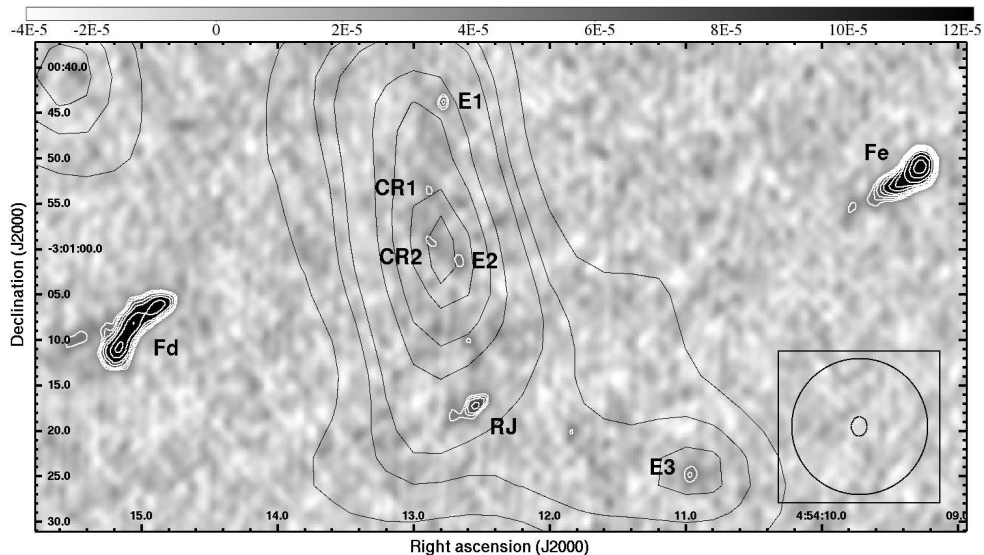
Figure 4.4: *VLA 1.4 GHz map derived from the A+B-array data set using* R = 0.6. *The greyscale has units of Jy beam^{-1}, and the corresponding contours (white) are drawn at -4, 4, 5, 6, 8, 10, 14, 18, 28, 48 & 78 times the 1σ noise level of 10.34 μJy beam^{-1}. The black lines (4, 6, 7, 9, 10, 11 & 11.5 mJy beam$^-$1) correspond to the SCUBA 850 μm contour map published in Borys et al. (2004a). A comparison of the beam size of both contour maps is shown in the bottom right corner: 2.14″×1.71″ at a position angle of −1°.43 for the radio map, and 15″×15″ for the sub-mm map.*

the sources are extended. In particular, RJ shows a bright elongated main body and an irregular 4σ extension towards the west. Note however, that the amorphous extensions present in the 2σ contours of E1, CR2 and E3 are not considered to be part of their real structure. In the following, references to the 2σ contours of these sources will implicitly exclude these amorphous extensions.

The peak positions and peak fluxes of all the radio detections were calculated with the task MAXFIT, which fits a quadratic function to a rectangular area that encloses the source (in our case, a rectangle delimited by the 2σ contours of the source). The total flux, on the other hand, was determined in two different ways: (i) by integrating the emission over the area defined by the 2σ contour of the source ($S_{2\sigma}$), and (ii) by adding the flux of all the clean components of the source model (S_{CC}). In this way, we can calculate the flux excess contained in the clean component model respect to the 2σ flux, which is an estimate of the amount of flux contained in the wings of the PSF-convolved sources below the 2σ contour.

The results obtained for the different parameters are listed in Table 4.1. Note that, since the cleaning procedure is stopped at certain flux level (half a sigma below the noise level), it is expected to have some left-over emission from the sources in the residual map, specially in the case of extended sources. To estimate this left-over flux, we have integrated the emission inside the 2σ contours of each source in the

residual map (see S_{resid} in Table 4.1). The results show that the S_{CC} for CR1 and RJ is underestimated by $\sim 6\%$, and by $\sim 10\%$ in the case of E2 and E3. The negative values for S_{resid} obtained for E1 and CR2 indicate that all the flux has been included in the CC model.

We also tried to characterize the properties of the six sources located within the sub-mm emission region by comparing them with Gaussians. The task JMFIT was used to fit simultaneously all the parameters of an elliptical Gaussian in the same rectangular area used with MAXFIT. Since the shape of RJ is far from being elliptical , we restricted the Gaussian fitting to the area that only contains the 2σ contours of the bright main body. The center and FWHM of the best fitting Gaussians are shown in Fig. 4.5.

The parameters derived from the best fits and their formal errors are listed in Table 4.2, where the sum of the square of the residuals is a measure of the relative goodness of the fit. As expected, the worst fits are obtained for RJ and E3, since they have the most irregular shapes. The best fits correspond to CR1 and E2, but note that the FWHM of the Gaussian in CR1 does not include the north-east 2σ extension.

When compared with Table 4.1, we see that the Gaussian fit provides basically the same estimates for the position (RA, DEC) and flux peak (S_{Pk}). The nominal integrated flux (S_{Gauss}) is in general larger than S_{CC} (except for E1), but consistent within the errors. The largest discrepancies are found for E3 and CR2 (see $\frac{S_{\text{CC}} - S_{\text{Gauss}}}{S_{\text{Gauss}}}$ in Table 4.1), probably because S_{Gauss} is including some flux from the 2σ amorphous extensions in these two sources that were not accounted for in the clean component model.

Finally, we would like to emphasize that, despite the faintness of CR1 and CR2 (SNR ~ 4.6), the histogram presented in Fig. 4.3 and the distribution of -4σ peaks in the final map (only a small number, located far away from the target region) suggests that they are real detections.

4.3.2   Disentangling the compact and extended radio emission

As can be seen in Fig. 4.6, the region between E1 and E2 shows an enhanced low level background when compared with the rest of the map, suggesting the presence of diffuse radio emission that has been partially resolved out. From now on, we will refer to this diffuse emission as the *extended component*, whereas E1, E2, E3, CR1 and CR2 will be consider *compact sources* by comparison.

If present, this extended component would only be detectable on short baselines, while the emission produced by compact sources will be picked up by all baselines at different resolution levels. Therefore, a map produced using only the short baselines does not permit us to distinguish between extended emission and a compact source observed at low resolution. The only way to isolate the extended component is by subtracting a model of the compact sources from the data.

Given the faintness of CR1 and CR2, and the complicated low level background in this region, the choice of boxes during the cleaning procedure becomes a highly subjective issue, and even the decision of cleaning CR1 and CR2 (and hence their CC models) can be questionable. For this reason, we produced a new version of the map presented in Fig. 4.4 (following the same procedure) in which CR1 and CR2 have not

Table 4.1: *Information about the identified radio sources in the core of MS0451.* The columns show: position (RA, DEC), peak flux density (S_{Pk}), total flux density inside the 2σ contour ($S_{2\sigma}$), total flux density obtained by adding the flux from all the clean components used to model the source (S_{CC}), total flux density inside the 2σ contour in the residual map (S_{resid}), comparison between the total flux derived from the CC model and the 2σ contours $\left(\frac{S_{CC}-S_{2\sigma}}{S_{2\sigma}}\right)$, comparison between the total flux derived from the CC model and the Gaussian fit $\left(\frac{S_{CC}-S_{Gauss}}{S_{Gauss}}\right)$ and signal-to-noise ratio (SNR). The quoted errors in RA and DEC correspond to the expected positional uncertainty of a point-like source in the map (FWHM/2 × SNR, were FWHM is the full width half maximum of the clean beam), while the error in the flux peak is estimated to be the same as the rms noise of the map. The error in the 2σ flux was calculated as $rms \times \sqrt{N}$, where rms is the rms noise of the map, and N is the number of beams within the area delimited by the 2σ contour of the source. The raw RJ bright lists the fluxes for RJ estimated without taking into account the 4σ west extension. Note that the positions listed here were derived before aligning the radio map respect to the HST image.

Name	RA ($+4^h\,54^m$) J2000 (sec)	DEC ($-3°$) J2000 (′, ″)	S_{Pk} (μJy beam^{-1})	$S_{2\sigma}$ (μJy)	S_{CC} (μJy)	S_{resid} (μJy)	$\frac{S_{CC}-S_{2\sigma}}{S_{2\sigma}}$ (%)	$\frac{S_{CC}-S_{Gauss}}{S_{Gauss}}$ (%)	SNR
E1	12.78 ± 0.01	00 : 43.8 ± 0.2	66 ± 10	42.5 ± 12	61.6	-1.4	45	17	6.4
CR1	12.88 ± 0.01	00 : 53.5 ± 0.2	47 ± 10	36.6 ± 12	47.2	2.9	29	-16	4.6
CR2	12.86 ± 0.01	00 : 59.3 ± 0.2	47 ± 10	43.8 ± 12	60.1	-0.1	37	-21	4.6
E2	12.66 ± 0.01	01 : 01.2 ± 0.2	51 ± 10	43.2 ± 12	52.0	5.1	20	-15	5.0
RJ bright	12.54 ± 0.01	01 : 17.2 ± 0.1	92 ± 10	121.2 ± 17	135.9	–	12	-17	8.9
RJ	12.54 ± 0.01	01 : 17.2 ± 0.1	92 ± 10	168.0 ± 22	195.3	10.5	16	–	8.9
E3	10.97 ± 0.01	01 : 24.8 ± 0.2	54 ± 10	63.3 ± 15	66.8	6.5	5	-28	5.2
Fd	15.162 ± 0.003	01 : 10.83 ± 0.05	199 ± 10	1180.9 ± 42	1260	29.5	7	–	19.2
Fe	09.2733 ± 0.0007	00 : 50.90 ± 0.01	1068 ± 10	1769.2 ± 34	1870	16.3	6	–	103.3

Table 4.2: *Gaussian fitting results for the identified compact radio sources in the core of MS0451. The columns show: position (RA, DEC), peak flux density (S_{Pk}), total flux density (S_{Gauss}), deconvolved Gaussian sizes (major axis, minor axis and position angle) with their corresponding formal errors, and the sum of the square of the residuals reported from the fit (SSR). Cases where the parameters of the Gaussian fits are not well constrained are indicated by a dash. Note that the positions listed here were derived before aligning the radio map with respect to the HST image.*

Name	RA ($+4^h\,54^m$) J2000 (sec)	DEC ($-3°$) J2000 (′, ″)	S_{Pk} (μJy beam^{-1})	S_{Gauss} (μJy)	Maj Axis (arcsec)	Min Axis (arcsec)	PA (deg)	SSR ($\times 10^{-9}$ Jy^2 beam^{-2})
E1	12.782 ± 0.007	$00:43.7 \pm 0.1$	66.1 ± 10.3	53.0 ± 15.5	0.00 ± 1.14	–	–	2.2
CR1	12.89 ± 0.01	$00:53.5 \pm 0.3$	45.6 ± 10.2	56.2 ± 20.4	1.87 ± 1.87	0.00 ± 1.17	31.4 ± 44.7	0.6
CR2	12.87 ± 0.01	$00:59.0 \pm 0.3$	45.9 ± 10.0	76.3 ± 24.5	2.28 ± 1.22	0.73 ± 0.99	37.6 ± 3.8	1.8
E2	12.67 ± 0.01	$01:01.2 \pm 0.2$	51.6 ± 10.3	61.2 ± 20.0	1.44 ± 1.44	0.00 ± 1.07	–	0.9
RJ bright	12.55 ± 0.01	$01:17.2 \pm 0.1$	82.9 ± 9.8	164 ± 27.6	3.02 ± 0.56	0.51 ± 0.73	128 ± 10.9	12.8
E3	10.95 ± 0.01	$01:24.8 \pm 0.2$	52.6 ± 9.9	92.5 ± 25.5	1.71 ± 0.95	1.58 ± 1.58	70.5 ± 39.0	3.4
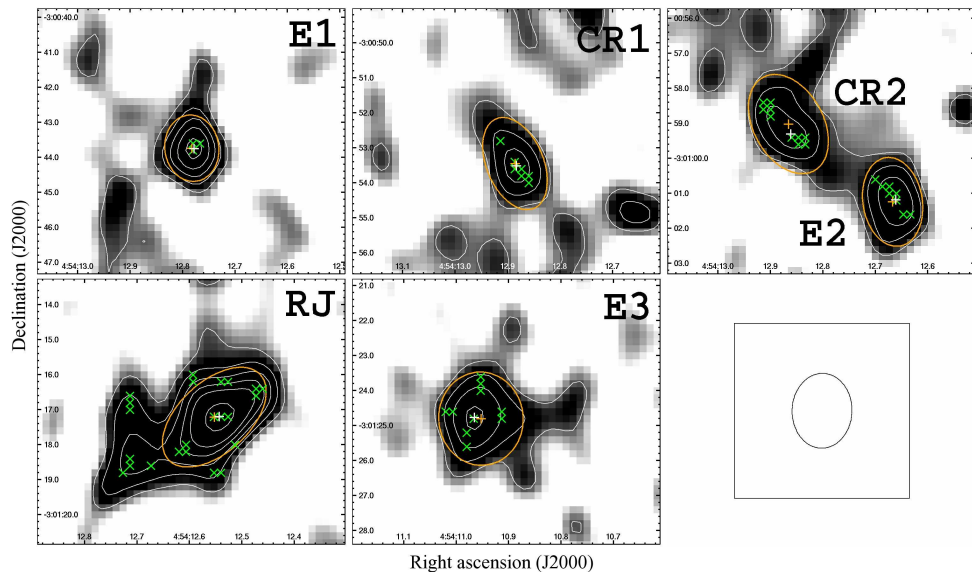
Figure 4.5: *Detail of the six radio sources located within the sub-mm emission region in Fig. 4.4. The white radio contours are drawn at 2, 3, 4, 5, 6 & 8 times the 1σ noise level of 10.34 μJy beam⁻¹. The radio peak positions (S_{Pk}) listed in Table 4.1 are indicated with white plus-symbols. The green crosses correspond to the positions of the clean components in each source model. Orange plus-symbols and ellipses represent the center and FWHM of the best fitting Gaussian for each source. A scaled version of the radio beam (2.14″ × 1.71″ at a position angle of −1°.43) is included in the bottom right panel.*

been cleaned. Then, we calculated S_{Pk}, $S_{2\sigma}$ and S_{CC} for all the sources in the new map, and compared them with the values presented in Table 4.1. In the case of E2 (which is the closest source to CR1 and CR2) we find differences of ∼ 10% for S_{CC} and ∼ 14% for $S_{2\sigma}$, whereas for the rest of the sources the differences in all three parameters are less than 7%. Since these variations are well withing the errors estimated for S_{Pk} and $S_{2\sigma}$ in Table 4.1, we can use the CC models of CR1 and CR2 presented in Fig. 4.5 without compromising the results.

Fig. 4.7 shows three ∼ 5″ resolution maps of the region between E1 and E2, produced by tapering the data with a Gaussian of FHWM = 30 kλ. In map (A) no compact sources were subtracted before the tapering and imaging. The central map (B) shows the result of subtracting the CC model of E1 and E2 from the data, and map (C) shows what is left after subtracting all the compact sources. Given the robust detection of a 6.6σ elongated source in panel (B), the presence of resolved extended radio emission in this region of the ∼ 2″ map (Fig. 4.6) is confirmed. Using the 2σ contour of map (B) as template, the integrated fluxes in panels (B) and (C) are $S_B = 173.52 \pm 26$ μJy and $S_C = 84.14 \pm 26$ μJy. The flux error was calculated as $rms \times \sqrt{N}$, where rms is the rms noise of the map, and N is the number of beams within the area delimited by the 2σ contour of map (B). These numbers indicate that
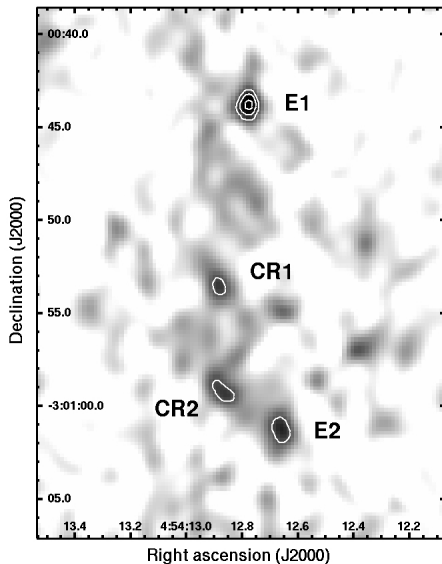
Figure 4.6: *Detail of Fig. 4.4. The greyscale has been modified to make more evident the low level background in this region of the radio map.*

∼ 50% of the flux in panel (B) has been included in the ∼ 2″ CC model of CR1 and CR2. Therefore, it seems that CR1 and CR2 constitute two relatively compact regions of an extended radio source located between E1 and E2. However, given the faintness of CR1, CR2 and the extended component in panel (C), deeper observations will be required to confirm this result.

Finally, to estimate the relative contribution of all the compact sources respect to the extended emission, we used the 2σ contour of map (A) as template to calculate the integrated flux of each map in Fig. 4.7: $S_A = 285 \pm 33$ μJy, $S_B = 204 \pm 33$ μJy and $S_C = 109 \pm 32$ μJy. The comparison of these fluxes indicates that 38% of the emission comes from an extended component, whereas 62% is produced by the compact sources (28% from E1 and E2, 34% from CR1 and CR2). As it will be discussed in detail in Sect. 4.4.1, the presence of this extended radio component constitutes a strong observational evidence in favor of the merger scenario proposed in B04.

4.4   Multi-wavelength Counterparts

Table 4.3 summarizes the relevant information about all the multi-wavelength data of MS0451 (optical, NIR and sub-mm) that we have collected from the literature to compare with our radio map. To identify possible counterparts of the radio sources, the radio and K′ band observations were aligned with respect to the HST image[5]. For

---

[5]astrometry matched to Subaru/Suprime-Cam observations of MS0451 for the PISCES survey (Kodama et al. 2005) using the IRAF package CCMAP.
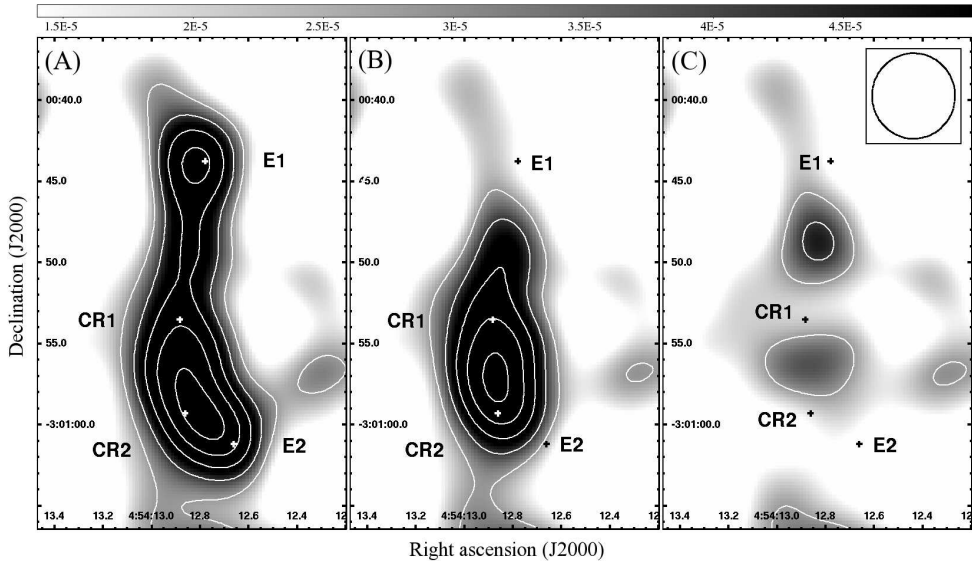
Figure 4.7: *VLA 1.4 GHz maps obtained by tapering the A+B-array data set with a Gaussian of FWHM = 30 kλ. The crosses indicate the positions of the radio detections identified in Fig. 4.4. Panel (A) includes all the emission between E1 and E2. In panel (B) the CC models of E1 and E2 were subtracted from the data before the tapering and cleaning procedure. Panel (C) shows what is left when CR1 and CR2 are also subtracted from the data. The greyscale has units of Jy beam^{-1}, and the corresponding contours are drawn at 2,3,4,5 & 6 times the 1σ noise level of 14 μJy beam^{-1}. The dimensions of the beam are 5.27″ × 5.12″ at a position angle of −88°.25 (panel (C), top right corner).*

.

Table 4.3: *Observations details. The columns show: Telescope and camera (Instrument), Frequency and filter indicated between parentheses (Freq.), Dates in which the observations were carried out (Obs. dates), total exposure time (Exp. time), depth of observations in magnitudes (depth) and references (Ref.)*

Instrument	Freq. (μm)	Obs. dates (dd/mm/yy)	Exp. time (ks)	depth (mag)	resolution (arcsecs)	Ref.
HST/ACS	0.83 (F814W)	–	2.4-2.7[1]	25	1.0	1,2
SUBARU/CISCO	2.13 (K′)	17-18/11/2000	9.22	22.1	0.6-0.8	3
JCMT/SCUBA	850	03/09/1998	22	–	15.0	4

Ref.: (1) Moran et al. (2007)[2]; (2) Smith et al., in prep.; (3) Takata et al. (2003); (4) Borys et al. (2004a).
[1] per pointing
[2] Further information on their wide field survey in MS0451 can be found in Chapter 2 of the PhD thesis of S. Moran. Survey data products from their wide field survey in MS0451 are available at http://www.astro.caltech.edu/ smm/clusters/
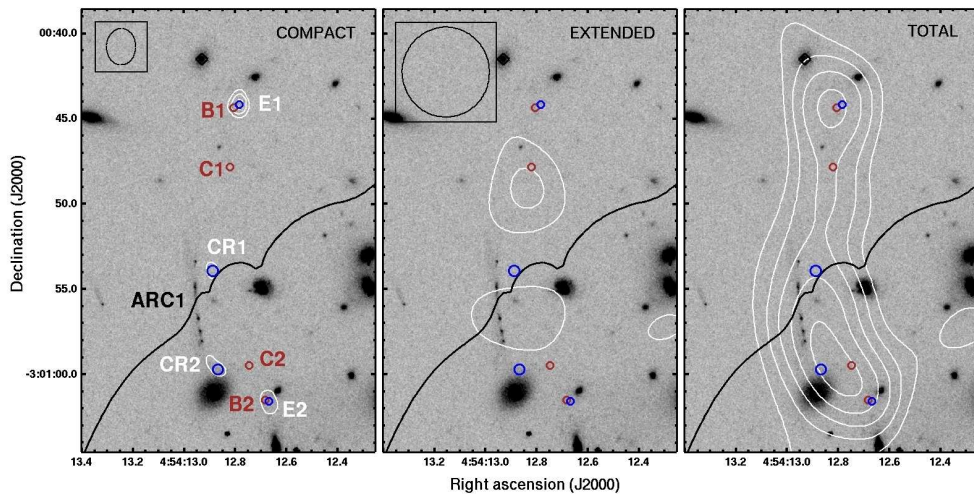
Figure 4.8: *Detail of the HST image in the arc region, including the critical curve at* z = 2.911 *predicted by the lens model described in Sect. 4.5 (black line). The red circles indicate the positions of the multiply imaged EROs mentioned in Borys et al. (2004a), whereas the blue circles correspond to the compact radio detections identified in this region. The radius of the circles indicate the estimated positional errors:* ∼ 0.20″ *for the EROs (astrometric error for the standard stars quoted in Takata et al. 2003), between* 0.1″ − 0.2″ *for the radio sources (see Table 4.1) and* ∼ 0.08″ *(half a pixel) for the optical sources. The contours correspond to the* ∼ 2″ *resolution radio map presented in Fig. 4.4 (left panel), and two of the* ∼ 5″ *resolution radio maps presented Fig. 4.7 (central and right panel).*

the alignment of the radio map we used 13 compact radio sources with reliable bright counterparts in the HST image, whereas 93 compact NIR sources were used to align the K′ band image. We find an rms scatter of 0.29″ between the radio map and the HST image, and 0.06″ between the K′ band and the HST images. Therefore, the inferred error in the alignment is $0.29/\sqrt{13} = 0.08″$ for the radio map and $0.06/\sqrt{93} = 0.006″$ for the K′ band image. These errors are negligible compared with the (relative) astrometric accuracy of the sources in each map, so they will be ignored in further analysis.

4.4.1   Comparison between radio and optical/NIR

Figures 4.8, 4.9 and 4.14 show different details of the HST image where the radio detections are located. The positions of the relevant sources are indicated with circles: blue for the radio sources and red for the K′ band sources. The counterparts of the sub-mm emission proposed by B04 have been indicated following the nomenclature introduced in Fig. 4.1. Note that the images B3 and C3 are supposed to be unresolved in the K′ band image presented in B04, and therefore referred to as B3/C3.

The relative position of the radio and NIR sources in these figures suggests that E1, E2 and E3 might be associated with B1, B2 and B3/C3. To better quantify these

associations, as well as identify other possible counterparts, we have used Bayesian inference to calculate the probability that the compact radio sources are physically associated with their nearest optical/NIR sources. The mathematical expression of this probability has been derived as follows.

Let $P(\mu|d)$ be the probability density of the true distance μ between two sources given an observed distance d. Following Bayesian inference, this probability is given by

$$P(\mu|d) = \frac{L(d|\mu)\,P(\mu)}{P(d)} \tag{4.1}$$

where $L(d|\mu)$ is the likelihood of the observed distance given a true distance, $P(\mu)$ is the probability density of the true distance before any measurement, and $P(d)$ is the probability density of the observed distance for all possible distances (a normalization constant).

As pointed out in Churchman et al. (2006), the likelihood of the observed distance between two sources which positions are described by a Gaussian distribution is not Gaussian. Instead, this likelihood in two dimensions is given by:

$$L(d|\mu) = \frac{d\,I_0\,(d\,\mu/(\sigma_1^2 + \sigma_2^2))}{\sigma_1^2 + \sigma_2^2}\,exp\left(\frac{-\mu^2 - d^2}{2\,(\sigma_1^2 + \sigma_2^2)}\right) \tag{4.2}$$

Where σ_1 and σ_2 are the errors in the position of each source, and I_0 is the modified Bessel function of integer order zero.

Since the area inside an annulus at radius μ increases as $\mu\,d\mu$, we assume that, for a source located at a random position, $P(\mu) = \mu$. Therefore:

$$P(\mu|d) \propto L(d|\mu) \cdot \mu \tag{4.3}$$

Which normalized gives:

$$B(\mu|d) = \frac{L(d|\mu) \cdot \mu}{\int_0^\infty L(d|\mu)\,d\mu} \tag{4.4}$$

The integral of this function between μ_1 and μ_2 gives the probability that, for a given pair of source centroids with observed offset d, the true distance between them lies between μ_1 and μ_2. Intuitively, one would say that the condition for two sources to be counterparts of each other is $\mu = 0$. The problem is that, in the case of extended sources like galaxies, the peak of emission at different wavelengths can be located at different positions, which means that $\mu \neq 0$ despite the fact that they are physical counterparts. For this reason, we will consider that a radio source has an optical/NIR counterpart when the centroid of the source emission lies inside the area of the optical/NIR source. The probability of meeting this condition is given by:

$$P_{assoc.} = \int_0^{r_{src}} B(\mu|d)\,d\mu \tag{4.5}$$

A list with the nearest optical/NIR sources of each radio detection, together with their associated probabilities, is presented in Table 4.4. As expected, only the images

Table 4.4: *Counterparts of the radio detections. The columns show: possible counterparts of the radio detections (Optical/IR source), measured offset between the radio source and the optical/IR source (d_{obs}), radius of the optical/IR source (r_{src}) and probability that the centroid of the radio source lies inside the area of the optical/IR source ($P_{assoc.}$). The coordinates of the counterpart sources can be found in tables 4.5 and 4.6. Sources which positions were taken from the K' band image are indicated with an asterisk (otherwise we used the HST coordinates). The positions of the radio sources used to calculate d_{obs} correspond to the values derived with* MAXFIT *in the aligned radio map.*

Radio source	Optical/IR source	d_{obs} (arcsecs)	r_{src} (arcsecs)	$P_{assoc.}$ (%)
E1	B1*	0.38	0.6	67.8
CR1	ARC 1.1	1.12	0.15	< 1
	ARC 2.1	1.40	0.25	< 1
	ARC 3.1	1.60	0.20	< 1
CR2	G2	1.39	0.70	< 1
	C2*	1.82	0.60	< 1
	ARC 1.2	1.92	0.15	< 1
E2	B2*	0.26	0.60	79.29
	G10	0.74	0.23	< 1
E3	4.3*	0.77	0.60	20.7
	5.3*	1.22	0.30	< 1
	G23	1.54	0.35	< 1
RJ	G8	1.91	0.30	< 1
	G11	2.40	0.26	< 1
	G14	1.39	0.60	< 1

of ERO B have a non-negligible probability of being associated with some of the radio sources (E1, E2 and E3). However, if E1, E2 and E3 are indeed the radio counterparts of B1, B2 and B3, they have to be multiple images produced by a radio source at $z \sim 2.9$. A quantitative analysis of this lensing scenario is presented in Sect. 4.5.4.

Finally, note that no optical/NIR counterpart has been identified with RJ. Therefore, given the depths of the optical and NIR images, it seems more likely that the extended morphology of RJ corresponds to an AGN rather than a resolved low redshift star forming galaxy. Within the AGN scenario, we expect that the peak of the radio emission corresponds to the position of an undetected optical source, and the extensions in opposite directions are two jets coming from it. Another conceivable scenario would be that the galaxy G14 is an AGN host with a one sided radio extension. However, the mayor axes of RJ does not seem to be aligned with G14, and this kind of AGN is not very common.

4.4.2   Comparison between radio and sub-mm

In this section, we will use the FIR-radio correlation to check whether the radio detections could be associated with the observed sub-mm emission. To make this kind of analysis, it is necessary to match the resolutions of the radio and sub-mm

observations. Therefore, the A+B array data was tapered with a Gaussian of 8.5 $K\lambda^6$ and restored with a clean beam of $15'' \times 15''$ at the end of the imaging process. The left panel of Fig. 4.11 shows the final tapered radio map (white contours) superimposed upon the sub-mm map (black contours) and the HST image of the cluster core. The positions of the detections in the high resolution radio map have been indicated with crosses as reference.

If all the observed sub-mm emission would be produced by a single SMG that does not host an AGN, it is expected that the radio and sub-mm morphologies would resemble each other. This is because the origin of the FIR-radio correlation seems to be linked to massive star formation (see page 24), which means that both the radio and sub-mm emission are originated in (approximately) the same regions of the galaxy. However, the $S_{850\mu m}/S_{1.4GHz}$ flux ratio observed in sub-mm galaxies displays a broad scatter which strongly depends on the characteristic dust temperature and the redshift (e.g Blain et al. 2002; Chapman et al. 2005). Therefore, if the observed sub-mm emission is being produced by several blended SMGs, we might find "morphological inconsistencies" like the one present in the left panel of Fig. 4.11 (note that the brightest peak of the radio emission is located in the region of RJ instead of been coincident with the brightest sub-mm peak).

Interestingly, if the CC model of RJ is subtracted from the data, the morphology of the radio emission becomes remarkably similar to the sub-mm emission (right panel of Fig. 4.11). This result strongly suggests that the source/sources responsible for the radio emission observed in this panel are also responsible for the bulk of the sub-mm emission. The other conclusion derived from this comparison is that, if RJ is contributing to the sub-mm emission, either its properties (redshift and/or dust temperature) are different from the properties of the source/sources associated with the other radio detections, or it has a "radio excess" due to an AGN.

Using 350 μm, 850 μm and 1.4 GHz observations of 15 bright SMGs with spectroscopic redshifts, Kovács et al. (2006) (K06 hereafter) conclude that the FIR-radio correlation remains valid for SMGs with $z \sim 1-3$ and luminosities between $10^{11} - 10^{13}$ M$_\odot$ (except when they are radio-loud AGN). To see how our system compares with this sample, we have made a more quantitative analysis of the FIR-radio correlation using the q_L parameter introduced in K06:

$$q_L = log\left(\frac{L_{FIR}}{[4.52 \text{ THz}] \text{ L}_{1.4GHz}}\right) \tag{4.6}$$

were total FIR luminosity is inferred from the flux density at 850 μm assuming a grey body model:
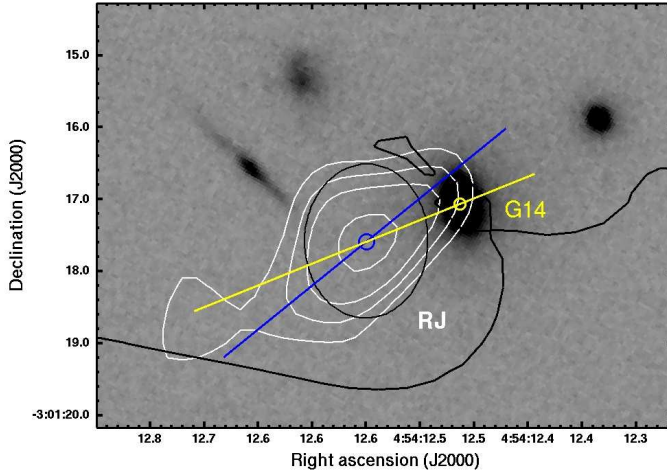
$$L_{FIR} = 4\pi D_L^2 \Gamma(4+\beta)\zeta(4+\beta)\left(\frac{kT_d}{h\nu}\right)^{4+\beta}\left(e^{h\nu/kT_d}-1\right)\nu S_{850\mu m} \tag{4.7}$$

and the radio luminosity can be derived as:

$$L_{1.4GHz} = 4\pi D_L^2 \, S_{1.4GHz} \, (1+z)^{\alpha-1} \tag{4.8}$$

---

[6]which corresponds to a clean beam of $15.78'' \times 14.65''$.

Figure 4.9: *Detail of the HST image in the region of RJ, including the critical curve at z = 2.911 predicted by the lens model describe in sect.4.4.1 (black line). The contours correspond to the ~ 2″ resolution radio map presented in Fig. 4.4. The radius of the circles show the estimated positional uncertainties: 0.1″ for RJ (see Table 4.1) and ~ 0.08″ (half a pixel) for G14. The blue line indicates the approximate orientation of the major axis of the radio source. For comparison, the yellow line shows the orientation of the RJ centroid respect to the galaxy G14. The black ellipse indicates the beam size of the radio map (2.14″ × 1.71″ at a position angle of −1°.43).*
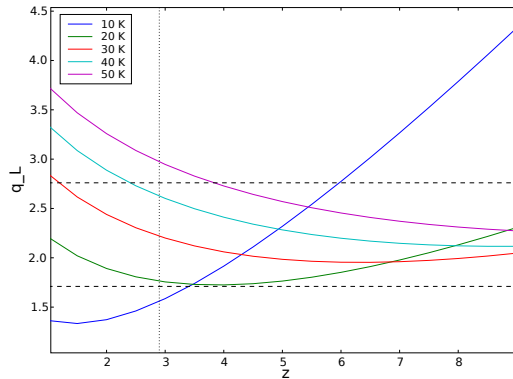
Figure 4.10: *Change of the parameter q_L with redshift for different characteristic dust temperatures. The horizontal dashed lines indicate the minimum and maximum value of q_L found in the SMG sample studied by Kovács et al. (2006). The dotted vertical line indicates the position of z = 2.9.*
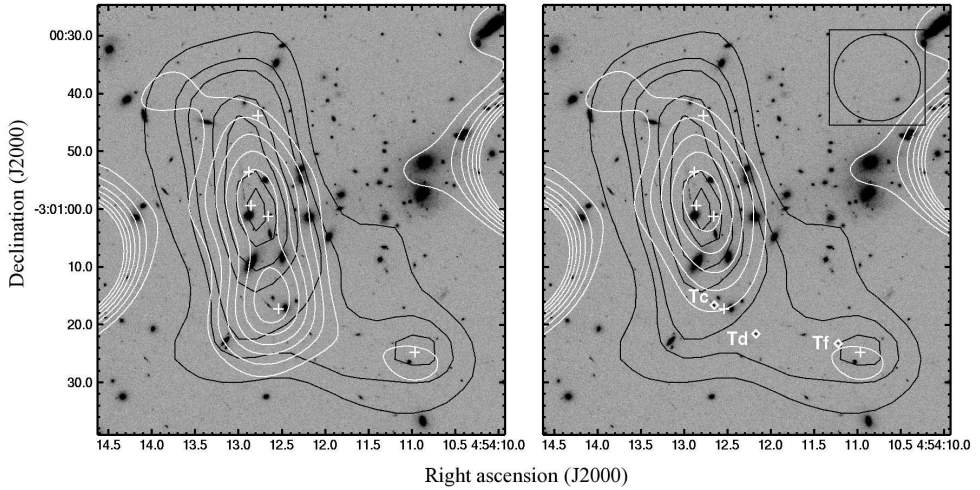
Figure 4.11: *Detail of the HST image of the cluster center, with the sub-mm 850 μm contour map superimposed in black. The white lines correspond to the VLA 1.4 GHz contour map obtained after tapering the A+B-array data to match the resolution in sub-mm. Radio contours are drawn at 2, 3, 4, 5, 6 & 7 times the 1σ noise level of 33.93 μJy beam^{-1}. Sub-mm contours are drawn at 4, 6, 7, 9, 10, 11 & 11.5 mJy beam^{-1}. The white crosses indicate the position of the radio sources identified within the sub-mm emission region. The beam size (15″ × 15″) is indicated in the top right corner. **Left panel:** map produced including all radio detections. **Right panel:** map produced after subtracting the CC model of RJ from the data. Indicated with diamonds are the positions of 3 EROs reported in Takata et al. (2003) that could be contributing to the observed sub-mm emission.*

In these formulas, D_{L} is the luminosity distance, β is the effective emissivity index (we assume $\beta = 1.5$), T_{d} is the characteristic dust temperature, ν corresponds to the observed sub-mm frequency, and α is the radio spectral index (we assume $\alpha = 0.7$).

At the position of the sub-mm peak, the radio and sub-mm fluxes were derived using the area delimited by the 3σ radio contour shown in the left panel of Fig. 4.11 ($S_{850\mu m} = 15.5 \pm 2.8$ mJy and $S_{1.4\mathrm{GHz}} = 241 \pm 42$ μJy). The different values of q_{L} derived from these fluxes as function of redshift and T_{d} are shown in Fig. 4.10. The horizontal dashed lines indicate the minimum and maximum value of q_{L} found in the K06 sample (discarding AGN hosts). Note that there is a wide range of z and T_{d} for which the observed fluxes are consistent with K06. If we now assume that the radio and sub-mm emission are produced by a (lensed) star forming galaxy at z = 2.9, only temperatures between $\sim 20 - 40$ K would be allowed, which is the temperature range in which most of the K06 sources lie.

Since AGNs do not follow the FIR-radio correlation, an estimate of the q_{L} value for RJ could provide extra evidence to confirm/discard the possible AGN nature of this source. However, that would require a higher resolution 850 μm map, to confirm the connection of RJ with a discrete sub-mm source and get an accurate estimate of its sub-mm flux. In addition, the redshift of RJ needs to be determined in order to

break the degeneracy between z and T_d illustrated in Fig. 4.10.

Finally, is important to mention that, although the energy output of the majority of SMGs is dominated by star formation, about $30 - 50\%$ host an AGN (Alexander et al. 2005). Therefore, even if the source associated with RJ is an AGN, it could still be contributing to the sub-mm emission observed in that region. Other potential contributors to the observed sub-mm emission are indicated in the right panel of Fig. 4.11.

4.5   Gravitational lens modeling of MS0451

In order to investigate the possible lensed nature of the radio detections, we used the publicly available LENSTOOL[7] code to model the mass distribution of the cluster. This modeling involves an optimization procedure, aimed to find the mass model parameter values that best reproduce the observational constrains (positions of the multiply imaged systems). For a detailed description of the strong lensing methodology followed in the LENSTOOL software we refer to Limousin et al. (2007), Jullo et al. (2007) and the appendix A2 of Smith et al. (2005).

The current best lens model of the cluster MS0451, published in B04 (B04 model hereafter), was produced with the first version of LENSTOOL (Kneib et al. 1993). This version is based on a downhill χ^2 minimization (which can be very sensitive to local minimum in the likelihood distribution), and does not provide estimates of the errors on the optimized parameters. The latest LENSTOOL version (Jullo et al. 2007) used in this Chapter includes a Bayesian Monte Carlo Markov chain (MCMC) optimization routine, which permits to determine errors in the optimized parameters and lowers the probability of ending in local χ^2 minimum.

4.5.1   Mass Model

The cluster mass model is constructed using two different components: (i) a cluster halo, which represents the DM component on cluster scales and the baryonic intracluster gas, and (ii) 27 galaxy halos that account for individual galaxies. Both components are described using a PIEMD profile (e.g. Limousin et al. 2005; Elíasdóttir et al. 2007), parametrized by position (RA, DEC), position angle (θ), ellipticity (ϵ), core radius (R_{core}), scale radius (R_{cut}) and velocity dispersion (σ_0). The density distribution for this profile is given by :

$$\rho(r) = \frac{\rho_0}{(1 + r^2/R_{core}^2)(1 + r^2/R_{cut}^2)} \tag{4.9}$$

The galaxy-scale component contains the cluster members located relatively close to the area were the multiple images are formed, because they are the ones that have the strongest effect in the potential of that region. We also included some fainter galaxies located close to the strong lensing constraints, since they are known to perturb the strong lensing configuration (Meneghetti et al. 2007). The details of our galaxy catalog are listed in Table 4.5, and their positions and sizes are displayed in

---

[7]http://www.oamp.fr/cosmology/lenstool/
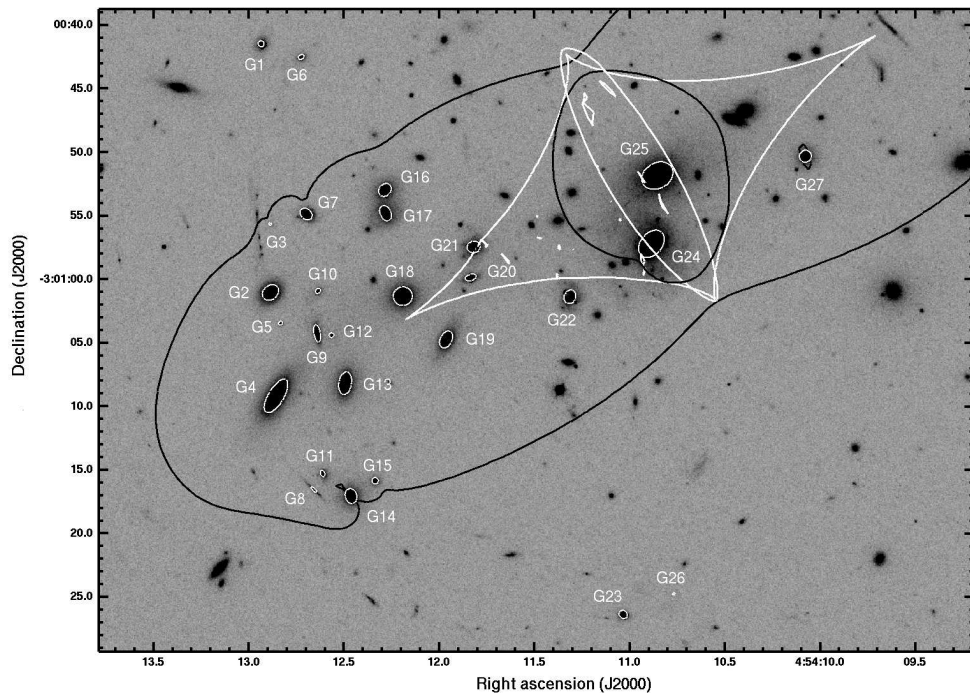
Figure 4.12: *Detail of the HST image of the cluster core, indicating all the galaxies that have been included in the lens model. The sizes of the ellipses correspond to the morphological parameters listed in Table 4.5. The lines represent the critical curves (black) and caustics (white) predicted by the lens model at z = 2.911.*

Fig. 4.12. Note that the galaxy catalog used in the B04 model (39 galaxies in total) includes cluster members located farther away, but not the faint galaxies mentioned before.

4.5.2 Multiple images

Figure 4.13 shows a close up of ARC1 as seeing on the ACS image. From its knotted structure we can identify 3 sets of mirror images, each of which should have its own counter-image. However, since it is not possible to distinguish the different knots in the de-magnified image of the arc (ARC1 ci, see Fig. 4.14), we assigned the same position to the counter-image of each set of constraints coming from the arc.

The positions for the EROs used in our model come from the Subaru K' band image published in Takata et al. (2003), which is deeper and has higher resolution than the CFHT K' band image published by B04. Based on their model, B04 identified the NIR source labeled B3/C3 as the result of the blending between the counter-images of B and C. However, we have detected a faint source (labeled '5.3' in Fig. 4.14) located very close to B3/C3 in the Subaru K' band image. This source was not reported in

Table 4.5: *Galaxy catalog for the new lens model of MS0451.* *The columns show: galaxy number (ID) galaxy coordinates (RA, DEC), semi-major axes (a), semi-minor axes (b), position angle (θ) and magnitude in the HST image (mag). An asterisk in the ID number indicate galaxies that were not included in the model presented in Borys et al. (2004a).*

ID	RA ($+4^h\,54^m$) J2000 (sec)	DEC ($-3°$) J2000 (′,″)	a (arcsec)	b (arcsec)	θ (deg)	mag (F814W)
01*	12.933	00 : 41.494	0.24	0.23	65	21.9511
02	12.884	01 : 01.056	0.70	0.55	40	20.1111
03*	12.886	00 : 55.685	0.12	0.09	-28	24.6286
04	12.855	01 : 09.205	1.50	0.60	59	19.0257
05*	12.831	01 : 03.476	0.17	0.15	55	23.2229
06*	12.723	00 : 42.529	0.24	0.17	30	22.3768
07	12.697	00 : 54.889	0.53	0.40	140	20.8427
08*	12.655	01 : 16.586	0.30	0.10	-44	22.5806
09*	12.639	01 : 04.288	0.70	0.25	-80	20.7576
10*	12.634	01 : 00.949	0.23	0.17	50	22.4744
11*	12.610	01 : 15.312	0.26	0.16	-69	22.1831
12*	12.563	01 : 04.426	0.19	0.19	20	22.5221
13	12.492	01 : 08.202	0.90	0.50	81	19.6345
14	12.461	01 : 17.075	0.60	0.45	105	20.0909
15*	12.334	01 : 15.892	0.25	0.25	-15	21.9945
16	12.283	00 : 53.001	0.55	0.45	50	20.3429
17	12.280	00 : 54.816	0.64	0.42	115	20.0471
18	12.189	01 : 01.348	0.75	0.73	10	19.5202
19	11.962	01 : 04.756	0.70	0.46	63	20.1070
20*	11.833	00 : 59.879	0.45	0.25	16	21.1736
21	11.817	00 : 57.484	0.53	0.45	15	20.3933
22	11.312	01 : 01.400	0.55	0.45	66	20.6069
23*	11.032	01 : 26.400	0.35	0.30	-40	21.4960
24	10.884	00 : 57.231	1.20	0.85	50	18.1360
25	10.853	00 : 51.865	1.30	1.00	30	18.1454
26*	10.767	01 : 24.772	0.12	0.08	21	25.2539
27	10.076	00 : 50.338	0.47	0.47	56	20.5351
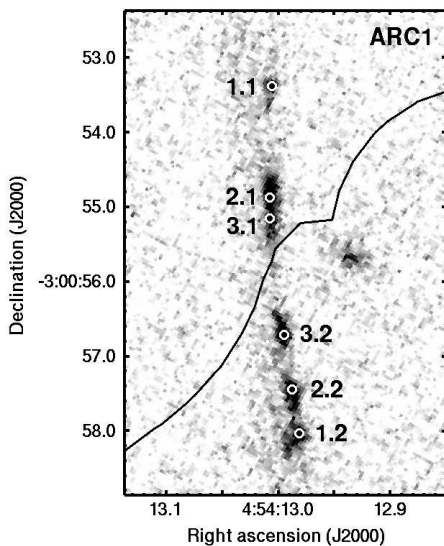
Figure 4.13: *Detail of the optical arc as seeing in the HST image. The circles indicate the positions of the three sets of mirror images listed in Table 4.6.*
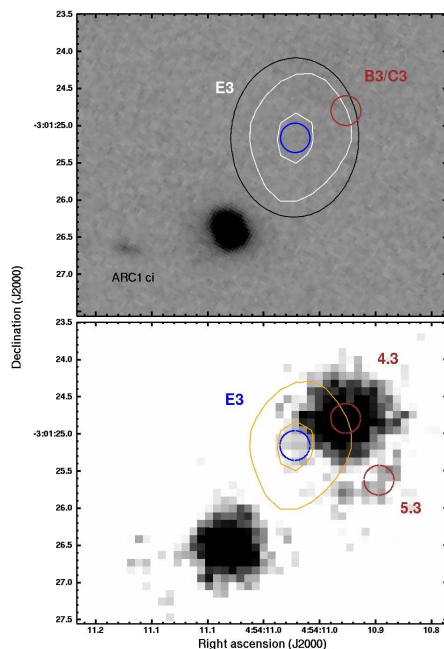
Figure 4.14: *Detail of the source E3, including its radio contours as presented in Fig. 4.4.* **Top panel:** *HST image of the region, including the positions of the counter images of the optical arc (ARC1 ci) and the ERO pair (B3/C3) reported by Borys et al. (2004a).* **Bottom panel:** *K' band image of the region, indicating the constraints used in the lens model (4.3 and 5.3). The radius of the circles show the estimated positional uncertainties: $\sim 0.20''$ for the K' band sources (astrometric error for the standard stars quoted in Takata et al. 2003), $0.2''$ for E3 (see Table 4.1) and $\sim 0.08''$ (half a pixel) for the optical sources. The black ellipse indicates the beam size of the radio map ($2.14'' \times 1.71''$ at a position angle of $-1°.43$).*

Table 4.6: *Constraints for the new lens model of MS0451. Sources used as constraints in the lens model presented by Borys et al. (2004a) are indicated with an asterisk in their ID number.*

Source name	ID	RA (+4^h 54^m) J2000 (sec)	DEC (−3°) J2000 (′,″)	Band
ARC1	1.1*	12.956	0 : 53.379	F814W
	1.2*	12.931	0 : 58.029	
	1.3*	11.124	1 : 26.641	
ARC1	2.1	12.958	0 : 54.869	F814W
	2.2	12.938	0 : 57.446	
	2.3	11.124	1 : 26.641	
ARC1	3.1	12.958	0 : 55.147	F814W
	3.2	12.945	0 : 56.710	
	3.3	11.124	1 : 26.641	
B1	4.1*	12.806	0 : 44.344	K′ band
B2	4.2*	12.684	1 : 01.488	
B3	4.3*	10.927	1 : 24.795	
C1	5.1	12.822	0 : 47.834	K′ band
C2	5.2	12.747	0 : 59.481	
C3	5.3	10.897	1 : 25.627	
RC1	6.1	12.890	0 : 53.907	1.4 GHz
RC2	6.2	12.868	0 : 59.696	

Takata et al. (2003) because it is too faint to be classified as a DRG[8] (T. Takata, private communication). Since it is possible that this source is the resolved counter-image of ERO C, we decided to include it as a constraint in the new model. The full set of constraints used for the optimization is listed in Table 4.6.

4.5.3   Optimization

The set of free parameters used during the optimization are: (i) all the parameters that characterize the cluster halo (except R_{core}) and (ii) the velocity dispersion (σ_0^*) and scale radius (R_{cut}^*) of a galaxy at z = $z_{cluster}$ with a typical luminosity L^* that corresponds to an observed magnitude of m = 18.8.

The σ_0 and R_{cut} of all the galaxy halos included in the mass model are derived from the luminosity of their associated galaxy using the following empirical scaling relations:

$$R_{cut} = R_{cut}^* \left(\frac{L}{L^*}\right)^{1/2} \qquad \sigma_0 = \sigma_0^* \left(\frac{L}{L^*}\right)^{1/4} \tag{4.10}$$

---

[8]Distant Red Galaxies, photometrically defined as $J - Ks > 2.3$.

Table 4.7: *Ranges in which the free parameters are allowed to vary during the lens model optimization. BCG is an abbreviation for Brightest Cluster Galaxy.*

Parameter	Opt. range
X	±6″ from BCG center
Y	±6″ from BCG center
ϵ	0 - 0.7
θ	0 - 180 deg
σ_0	900 - 1800 km/s
R_{core}	30 - 120 kpc
σ_0^*	120 - 140 km/s
R_{cut}^*	30 - 180 kpc

The scaling relation for σ_0 assumes that mass traces light, and its origin resides in the Tully-Fisher and Faber-Jackson relations. The scaling relation for the radial parameter assumes that the mass-to-light ratio is constant for all galaxies. The zero point of these relations is set by the magnitude of the L^* galaxy. The rest of the parameters of all galaxy halos (RA, DEC, θ and ϵ) are fixed to the values measured from the light distribution of the related galaxy, while their R_{core} is set to zero.

The ranges in which the free parameters are allowed to vary during the optimization are listed in Table 4.7. Note that the scale radius describes the properties of the mass distribution on scales much larger than the radius over which the multiple images can be found. Therefore, since strong lensing cannot give any reliable constrains on this parameter, its value is set to an arbitrary large number (1500 kpc). The ranges adopted for the L^* galaxy are motivated by galaxy-galaxy lensing studies in clusters (Natarajan et al. 1998, 2002a,b; Limousin et al. 2007).

Since the redshift of the EROs has not been confirmed spectroscopically, the modeling procedure was carried out in four steps. In the first step, only the sets of images from ARC1 at z_{spect} = 2.911 where used as constraints in the optimization. The resultant best model was then re-optimized, including the constraints provided by ERO B but leaving z_B as free parameter. As a result, the predicted redshift of ERO B is z_B = 2.93 ± 0.13. In the third step, the constraints from ERO C were used in a new re-optimization of the best model obtained in the previous step, assuming z_B = 2.9 and leaving z_C as free parameter. This provides a z_C = 2.85 ± 0.06, which is the same redshift that B04 derived for the ERO pair. In the final step, the previous best model is re-optimized (in the *image* plane) including all the constraints with z = 2.911.

The Bayesian MCMC optimization routine included in the new version of LENSTOOL provides two kinds of outputs: (i) the likelihood of reproducing the observed constraints, independently derived for each free parameter of the mass model, and (ii) the set of model parameters that provides the best fit to the input data. The most likely values for the model parameters obtained from these histograms are listed in Table 4.8, whereas the parameters of the best model (MFINAL hereafter) are listed in Table 4.9. The image positions are well reproduced, with image plane positional

Table 4.8: ***Most likely mass model parameters.*** *The columns show: position respect to the brightest cluster galaxy (X,Y), ellipticity of the mass distribution (ϵ, expressed as $a^2 - b^2/a^2 + b^2$, were a and b are the semi-major and semi minor axes of the ellipse that describes the light distribution of the clump), position angle (θ), velocity dispersion (σ_0), core radius (r_{core}) and scale radius (r_{cut}). Error bars correspond to 1σ confidence level as inferred from the MCMC optimization. Values into brackets are not optimized. When the posterior distribution is not Gaussian, we report the mode and asymmetric error bars. The coordinates of the brightest cluster galaxy are RA = $4^h54^m10.87^s$, DEC = $-3°0'54.00''$.*

Clump	X ('')	Y ('')	ϵ	θ (deg)	σ_0	r_{core} (kpc)	r_{cut} (kpc)
Cluster	$-0.5^{+4.1}_{-1.2}$	2.7 ± 1.5	$0.69^{+0.0}_{-0.1}$	31.3 ± 1.1	1144.8 ± 36	60.8 ± 24	[1 500]
L* elliptical galaxy	–	–	–	–	135.1 ± 43.9	[0]	$30.1^{+43.6}_{-4.9}$

Table 4.9: ***Best mass model.*** *The columns show: position respect to the brightest cluster galaxy (X,Y), ellipticity of the mass distribution (ϵ, expressed as $a^2 - b^2/a^2 + b^2$, were a and b are the semi-major and semi minor axes of the ellipse that describes the light distribution of the clump), position angle (θ), velocity dispersion (σ_0), core radius (r_{core}) and scale radius (r_{cut}). Values into brackets are not optimized. The coordinates of the brightest cluster galaxy are RA = $4^h54^m10.87^s$, DEC = $-3°0'54.00''$.*

Clump	X ('')	Y ('')	ϵ	θ (deg)	σ_0 (km/s)	r_{core} (kpc)	r_{cut} (kpc)
Cluster	-0.77	2.26	0.70	31.15	1117.32	7.67	[1 500]
L* elliptical galaxy	–	–	–	–	150.42	[0]	3.88

rms differences between $\sim 0.1''$ and $0.3''$ (see Table 4.10). The projected mass within the Einstein radius (here approximated by the ARC1 distance from the center, is $M_{2D}\,(30'') = 1.73 \times 10^{14}\,M_\odot$.

4.5.4   Analysis of the radio data using the new lens model

Since CR1 and CR2 are located in a region with several multiply-imaged systems (see Fig. 4.8), it is conceivable that they might also constitute a set of mirror images. To test this hypothesis, we redo the optimization using the positions of these two radio sources as an additional set of constraints (system 6, see Table 4.6), first assuming $z_{CR} = 2.911$ and then considering z_{CR} as a free parameter. A summary of the properties of the resultant best models (MZFIX and MZFREE hereafter) is presented in Table 4.10 and Table 4.11.

The optimization with z free results in a predicted redshift for system 6 of $z_{CR} = 2.4 \pm 0.074$, which is not consistent with $z = 2.911$. If we compare the probability of

Table 4.10: *Results of the best models for each set of constraints. The columns show: ID of each set of constraints (System), reduced χ^2 obtained for each model (χ^2 final, zfix and zfree) and average separation between the observed and predicted position of the lensed images for each model (rms final, zfix and zfree).*

System	χ^2 MFINAL	χ^2 MZFIX	χ^2 MZFREE	rms MFINAL	rms MZFIX	rms MZFREE
1	3.89	6.71	4.04	0.34	0.45	0.35
2	2.02	0.68	1.28	0.25	0.14	0.20
3	1.33	0.74	0.95	0.20	0.15	0.17
4	3.86	8.53	6.32	0.34	0.51	0.44
5	0.50	1.48	0.62	0.12	0.21	0.14
6		35.46	3.70		1.26	0.41

Table 4.11: *General results of the best models. The columns show: Nickname of the model (Model), sum of the reduced χ^2 of all the optical/NIR sets of constraints (χ^2 optical), reduced χ^2 for the radio set of constraints (χ^2 radio), average separation between the observed and predicted position of all the lensed images used as constraints (aver rms), probability of the model to reproduce the observations (log(evidence)).*

Model	χ^2 optical	χ^2 radio	aver rms	log(evidence)
MFINAL	11.60	–	0.26	-24.503
MZFIX	18.14	35.46	0.53	-45.340
MZFREE	13.21	3.70	0.30	-29.741

MZFIX and MZFREE to reproduce the observations (the evidence, see Table 4.11), it is clear that MZFREE is preferred over MZFIX. Note also that the rms difference between the observed and predicted image positions for system 6 is three times worse for MZFIX compared with MZFREE (see Table 4.10). On the other hand, the total χ^2 of MZFREE for all the optical/IR multiply imaged systems (χ^2 optical, see Table 4.11) is just slightly worse that the corresponding χ^2 of MFINAL, which means that MFINAL and MZFREE are equally good. Note that the evidence cannot be used to compare these two models because the number of free parameters in each of them is different.

Therefore, unless the positional uncertainty of CR1 and CR2 could be as large as $\sim 1''$ (which seems unlikely, since the positional error for these sources derived from the observations is $0.2'' - 0.3''$), these results indicate that the lens model favors an scenario in which CR1 and CR2 (if assumed to be mirror images) are produced by a radio source that is not located at the same redshift as the optical arc. However, as discussed in Sect. 4.3.2, CR1 and CR2 seem to be two relatively compact ($\sim 2''$) regions of an extended ($\sim 5''$) radio source. Therefore, it is possible that this extended radio emission is a multiply imaged structure produced by a source at z = 2.9, in which CR1 and CR2 are not mirror images. Until the structure of this extended radio emission can be robustly mapped with deeper observations and included in
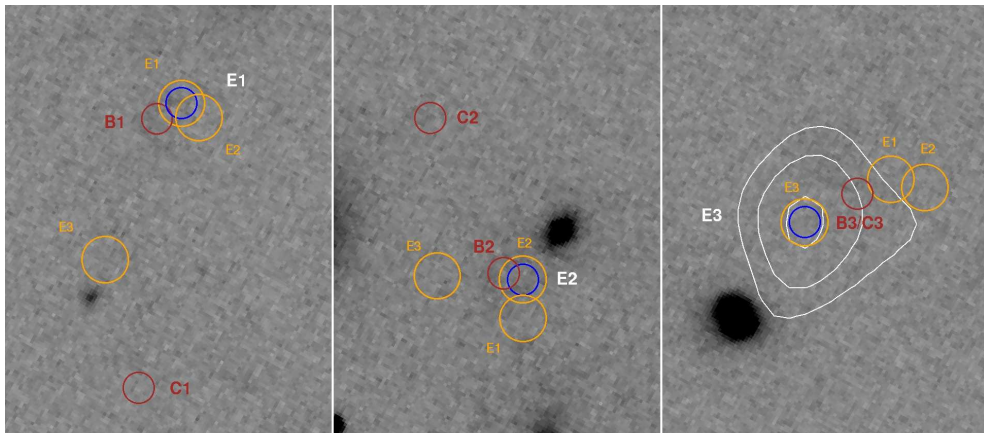
Figure 4.15:   *Analysis of the lensing nature of E1, E2 and E3 with the lens model* MFINAL. *The orange circles indicate the image positions predicted after tracing each of the three radio sources independently into the source plane and lens them back into the image plane. The radius of the circles correspond to* 0.3″. *The rest of the labels are the same used in Fig. 4.8.*

the modeling process, the possibility that CR1 and CR2 are associated with a lensed source at redshift 2.9 remains open.

As mentioned in Sect. 4.4.1, the multiple images of ERO B have a non-negligible probability of being associated with the radio detections E1, E2 and E3. However, the probability that E3 and B3/C3 are associated is significantly lower than for E1-B1 and E2-B2. For this reason, we used MFINAL to check if the positions of E1, E2 and E3 would be consistent with a set of three images produced by a radio source at z = 2.9. This was done in the following way: for each radio detection, its position was traced back into the source plane, and the resultant source was lensed again into the image plane. In this way, the model provided three predicted positions for each radio source, one of them being the position used as input.

The results (shown in Fig. 4.15) indicate that E3 cannot be interpreted as the radio counterpart of B3/C3, since the images produced by E1 and E2 in the counter image region are located on the right side of B3/C3 (unlike in the case of E1 and E2), at a distance which is inconsistent with the average rms of MFINAL. A possible scenario that can explain this result is that E1 and E2 are multiple images (but we don't detect the associated counter-image because it is too faint) and E3 is a non-lensed radio galaxy that it is serendipitously lying in this region. However, as it will be discussed in the next section, it is also possible to explain E3 as a lensed image produced by a source at z = 2.9 under the merger scenario proposed in B04.

4.6   Discussion: the merger scenario

Figure 4.8 shows a detail of the HST image at the position of the sub-mm peak, where ARC1 and the EROs are located. The contour map of the right panel indicates the total radio emission observed in this region, whereas the left and central panels show the compact and extended component. The black line correspond to the critical curve at $z = 2.9$ predicted by the lens model of the cluster described in Sect. 4.5.

If ARC1 and the EROs are indeed multiple images produced by three different regions of a merger at $z = 2.9$, the rest of the merger lying between them should also be multiply-imaged. Hence, if the merger contains a lot of dust (as expected from a high-z SMG), this images would not be seen in the optical, but they would show up in the radio.

Under this scenario, the fact that CR1 and CR2 do not seem to have optical counterparts, and lie in the region between ARC1 and the ERO images, suggests that they could be lensed images associated with the highly-obscured center of the merger. However, as discussed in Sect. 4.5.4, they can also be interpreted as a set of mirror images produced by another radio galaxy located at a different redshift. The real strong evidence in favor of the merger hypothesis comes from the extended component in which CR1 and CR2 seem to be embedded, which provides 38% of the observed radio flux in the region of the sub-mm peak. As is clearly shown in the central panel of Fig. 4.8, this extended component constitutes a bridge of emission between the compact radio sources, as expected from the multiply imaged dust-obscured material of the merger located between the optical and NIR emitting regions. In complete agreement with this scenario, the shape of the total radio emission in the right panel of Fig. 4.8 follows the distribution of the optical arc and the ERO images remarkably well.

In this case, we can also expect the extended emission to be multiply imaged like ARC1 and the EROs, producing a counter-image in the region between ARC1 ci and B3/C3 (see Fig. 4.14). Since the images in this region are de-magnified, it is likely that the expected radio counterpart of B3/C3, and the counter image associated with the extended emission, are blended. That would shift the peak of the total observed radio emission towards ARC1 ci, explaining why the probability derived for E3-B3/C3 is much lower than what it is found for E1-B1 and E2-B2.

Finally, it is also not surprising that E1-B1 and E2-B2 are not identified as robust ($\geq$ 95%) counterpart pairs. With the cluster magnification generating a high resolution (distorted) view of the inner structure of the merger, the observed offset between E1-B1 and E2-B2 could be real, indicating that the NIR and radio emissions are arising from slightly different regions inside the merger.

4.7   Summary and Conclusions

SMM J04542−0301 is an elongated region of bright sub-mm emission located in the core of the cluster MS0451.6−0305. It has been suggested (Borys et al. 2004a) to be partially produced by a multiply-imaged z = 2.9 merger which contains a LBG (lensed as ARC1 and ARC1 ci), and two EROs (lensed as B1, B2, C1, C2 and B3/C3). Given the low resolution and poor positional accuracy of the sub-mm map, it is very difficult to confirm the connection between SMM J04542−0301 and the optical/NIR lensed images. However, high resolution radio interferometric observations can help to establish this connection thanks to the FIR-radio correlation, which has being found to be valid for SMGs (Kovács et al. 2006; Vlahakis et al. 2007; Ibar et al. 2008; Michałowski et al. 2009).

In Chapter 3, we reported on the detection of 1.4 GHz radio emission coincident with this system using VLA archival data. Now, following a more sophisticated data reduction procedure, the previous B-array observations have being re-reduced and combined with new high resolution A-array observations. The resultant data set has been used to produced two radio maps of the cluster core:

(i) A deep ($\sim 10\ \mu$Jy), high resolution ($\sim 2''$) map, to compare with the optical/NIR images. In this map we have detected 5 sources (E1, E2, CR1, CR2 and E3) located near the optical/NIR lensed images, and one source (RJ) located in the central region of the sub-mm emission (see Fig. 4.4). Despite the fact that some of the sources have SNR < 5, the fact that the -4σ peaks lie far from the central target region adds confidence to the reality of the sources.

(ii) A 15$''$ resolution map, to compare with SMM J04542−0301 (see Fig. 4.11).

The source RJ is the brightest and most extended of these six detections, with no obvious counterpart in the optical/NIR. Although its extended morphology could be interpreted as an AGN signature, the degeneracy between redshift and dust temperature permits the observed $S_{850\mu m}/S_{1.4GHz}$ at the position of RJ to be consistent with a starforming SMG that follows the FIR-radio correlation. In any case, the low resolution of the 850 μm map makes impossible to determine if RJ is really contributing to the observed sub-mm emission in this region.

On the other hand, the other five radio detections constitute a strong observational evidence in favor of the merger scenario proposed by Borys et al. (2004a). The evidence that supports this conclusion can be summarized as follows:

- If the optical arc and the EROs are multiple images produced by three different regions of a merger at z = 2.9, the dust obscured material between these regions is expected to be lensed in the same way, but only visible at radio and sub-mm. In agreement with this scenario, the shape of the radio emission observed at the sub-mm peak follows the distribution of the optical arc and the ERO images remarkably well (Fig. 4.7).

- CR1 and CR2 do not have any optical/NIR counterpart. However, they seem to constitute two relatively compact emitting regions embedded in a $\sim 5''$ extended source located between E1 and E2. The presence of this extended component (which contributes 38% of the total radio flux in the sub-mm peak) can only be explained if it is being produced by the dust obscured lensed material in the center of the merger.

- The compact sources E1 and E2 have a high probability of being associated with the images of ERO B, but this probability is considerably lower for E3-B3/C3. A plausible explanation of this result can be provided by the merger scenario, in which the lensed extended component is expected to have a counter image which would be blended with the radio emission associated with E3/C3. This would shift the position of the total observed peak, lowering the probability of identifying E3 and B3/C3 as counterparts.

- The fact that B1, B2 and B3/C3 are not robust ($\geq$ 95%) counterparts of E1, E2 and E3, indicates that the radio and NIR emission is being produced at slightly different positions in the sources plane, which can be distinguished thanks to the enhanced resolution provided by the lensing magnification.

- If the $15''$ resolution radio map is produced after the CC model of RJ is subtracted from the data, its morphology turns out to be remarkably similar to the sub-mm map (right panel of Fig. 4.11). This result strongly suggests that the sources E1, E2, CR1, CR2 and E3 are associated with the extended sub-mm emission, allowing us to establish a direct link between SMM J04542−0301 and the merger.

In this Chapter we have also presented a new lens model of the cluster MS0451.6 −0305, produced with the latest version of the LENSTOOL code (Jullo et al. 2007), in which the positions of the ERO images and the arc knots have been used as constrains. The redshifts of the EROs predicted by this model are $z_B = 2.93 \pm 0.13$ and $z_C = 2.85 \pm 0.06$, in agreement with Borys et al. (2004a).

Including the positions of CR1 and CR2 as mirror images in the model significantly degrades the overall rms of the optimization. However, since these two sources are embedded in an extended source (which cannot be included in the lens model due to the current limitations of the LENSTOOL code), it is very difficult to establish a one-to-one identification of structures in the image plane. Therefore, the possibility that CR1 and CR2 are lensed images produced by the dust-obscured core of the merger remains open.

Acknowledgments